Received: 29 October 2021 | Revised: 14 May 2022 | Accepted: 20 May 2022

DOI: 10.1002/joc.7736

RESEARCH ARTICLE

International Journal of Climatology RMetS

Coupled Model Intercomparison Project phase 5 and 6 representation of peak and end of rainy season over Upper Blue Nile basin

Zewdu Alamineh Fetene[1,2,3] | **Benjamin F. Zaitchik**[2] | **Tadesse Terefe Zeleke**[4] | **Baylie Damtie Yeshita**[5,6] | **Amandeep Vashisht**[2]

[1]Department of Atmospheric Physics, Bahir Dar University, Bahir Dar, Ethiopia

[2]Department of Earth and Planetary Sciences, Johns Hopkins University, Baltimore, Maryland, USA

[3]Department of Physics, Debre Tabor University, Debre Tabor, Ethiopia

[4]Institute of Geophysics, Space Science and Astronomy, Addis Ababa University, Addis Ababa, Ethiopia

[5]Washera Geospace and Radar Science Laboratory, Bahir Dar University, Bahir Dar, Ethiopia

[6]Kepler, Kigali, Rwanda

Correspondence
Zewdu Alamineh Fetene, Department of Atmospheric Physics, Bahir Dar University, Bahir Dar, Ethiopia.
Email: alamineh.zewdu36@gmail.com

Funding information
U.S. National Science Foundation (NSF), Grant/Award Number: ICER-1624335

Abstract

The Upper Blue Nile river basin (uBN) is vital to three countries' water, food, and energy security (Ethiopia, Sudan, and Egypt). It is also a region with substantial interannual precipitation variability and the potential for significant climate change in coming decades. The El Niño–Southern Oscillation (ENSO) affects both variability and trends in uBN precipitation, with El Niño episodes historically connected with below-average rainfall. In this context, this study seeks to: (a) examine the representation of ENSO–uBN rainfall teleconnections in simulations from the sixth Coupled Model Intercomparison Project (CMIP6), as compared to the previous generation of models (CMIP5); (b) distinguish between teleconnections during the peak of the rainy season (July–August [JA]) and the agriculturally critical end-of-season rains (September–October [SO]); (c) investigate evidence for Tropical Easterly Jet (TEJ) mediation of these teleconnections in CMIP6 versus CMIP5 and for both peak rains and end of the rainy season. Using a subset of high performing models, we find that CMIP6 simulations of uBN precipitation show somewhat less bias than CMIP5 for JA total rainfall, and that correlations with ENSO have become more consistent across models, but that differences between CMIP5 and CMIP6 are modest. CMIP6 simulations, like CMIP5, overestimate SO rainfall and suggest a stronger ENSO association in SO than is indicated by observations. Model representation of the TEJ and its association with both ENSO and uBN precipitation show no systematic change between CMIP5 and CMIP6. The mediating influence of the TEJ appears to be more important in JA than SO.

KEYWORDS

CMIP, ENSO, mechanism, precipitation, Upper Blue Nile basin

1 | INTRODUCTION

The coupled model intercomparison projects (CMIP; Eyring *et al.*, 2016; Baker and Huang, 2014) coordinate leading climate modelling institutions to perform a suite of consistent general circulation model (GCM) simulation experiments. These experiments are used to study sensitivity of the climate system, to understand GCM performance and capabilities, to simulate past climates, and, in perhaps their most widely used application, to make quantitative climate

forecasts for the 21st century (Miao *et al.*, 2014; \Yang *et al.*, 2018). Despite the well-documented limitations of GCMs for providing localized climate information or for representing precipitation processes (IPCC, 2013; Otieno and Anyah, 2013; Jury, 2015), many projections of climate change impacts on hydrology rely on the CMIP GCM realizations as a direct or indirect source of precipitation estimates (Kitoh and Endo, 2016), and these estimates carry through to estimates of future climate change impacts on environment, water resources, and agriculture (Kundzewicz *et al.*, 2008; Chen *et al.*, 2011; Sivakumar, 2011). The implications of relying on GCMs for these projections are particularly acute for Africa, where progress on GCM representation of relevant climate dynamics and climate variability has been limited (Zappa *et al.*, 2013; Bhattacharjee and Zaitchik, 2015; Vashisht *et al.*, 2021).

In assessing the reliability and usefulness of GCM projections for applications in Africa, it is useful to consider the models' ability to capture large-scale climate features relevant to climate variability and change. Even when coarse spatial resolution and biases in parameterized processes limit the fidelity of a GCM's simulation of rainfall in a specific location, for example (Dibike and Coulibaly, 2006; Bokke *et al.*, 2017), it is possible that the model captures large-scale atmospheric dynamics that drive rainfall variability at that location. This information can be applied to climate analysis and projections when GCM results are used in concert with appropriate bias correction and downscaling techniques (Wilby and Wigley, 1997; Chen *et al.*, 2012). Conversely, if a GCM is unable to capture the key large-scale drivers of climate dynamics in a given region then its projections will be suspect, even if the model has relatively low bias in metrics like mean annual precipitation at a site of interest.

In this paper we study the representation of large-scale climate models and teleconnections relevant to the Upper Blue Nile basin (uBN) in the latest generation of CMIP simulations (CMIP6; Eyring *et al.*, 2016). Specifically, we have compared CMIP6 to the previous generation of models, CMIP5, focusing on models that provided reasonably realistic performance for this region in CMIP5. This allows us to address the question of whether there has been any systematic improvement among the leading models for uBN applications between CMIP5 and CMIP6. As rainfall in the uBN is highly sensitive to the El Niño–Southern Oscillation (ENSO; Abtew *et al.*, 2009; Emile-Geay *et al.*, 2013; Zaroug *et al.*, 2014; Le *et al.*, 2020; Vashisht *et al.*, 2021), we focus on model representation of the ENSO influence on uBN rainfall, including the intermediate question of how each model captures ENSO influence on the Tropical Easterly Jet (TEJ), which has been hypothesized to be a driver of interannual precipitation variability in this region (Gleixner *et al.*, 2017; Vashisht *et al.*, 2021), and how TEJ variability projects onto uBN rainfall variability. We consider the main rainy season in the uBN and divide the analysis into the period of peak rainfall season (July–August) and the late rainy season (September–October), which is critical for agricultural activities and is highly variable between years (Berhane *et al.*, 2014).

2 | DATA AND METHODOLOGY

2.1 | Study area

The uBN is one of Ethiopia's most important food-producing basins. It is the Nile River's single largest source of water, making it important for both large-scale hydropower and irrigation, as well as a vast population of subsistence farmers (Conway and Hulme, 1993; Sutcliffe and Parks, 1999). The boreal summer rainfall (Figure 1), which peaks in July and August (hereafter referred to as JA) and concludes in September and October (hereafter referred to as SO), is extremely important to the uBN. The uBN experiences substantial interannual climate variability, which can have negative impacts on local agriculture (Zaitchik *et al.*, 2012) and major implications for regional food security (Berhane *et al.*, 2014) and transboundary hydroeconomics (Block and Strzepek, 2012).

For this study, we approximate the uBN area with a box of 7.5°–12.5°N, 33.5°–40°E. We aggregate JA precipitation to represent "peak rainy season" conditions, and we aggregate SO precipitation to capture the end of the rainy season. Though June is typically included in analyses of uBN summer rainfall, here we focus on JA and SO because June is considered to be a transition month (Nicholson, 2014) and was shown to have weak relationship with ENSO variability by Berhane *et al.* (2014).

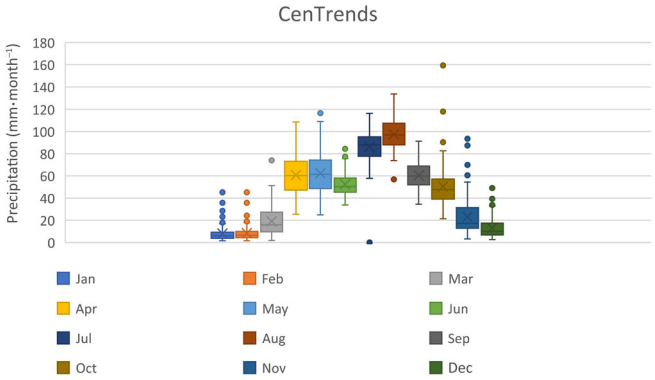

FIGURE 1 Monthly precipitation in the uBN, based on CenTrends data for 1950–2005

2.2 | Observational data

We draw precipitation data from the CenTrends dataset (Funk *et al*., 2015a; 2015b) which provides a reasonably complete and accurate gridded precipitation product for east Africa (15°S–18°N, 280°–54°E) with 0.1° resolution from 1900 to 2014. The Extended Reconstructed Sea Surface temperature version 3b (ERSSTv3b; Smith *et al*., 2008) monthly values are used for observed sea surface temperature (SST). We used monthly precipitation throughout the year to examine seasonality in GCMs relative to observations.

For the observational record, El Niño (La Niña) events were defined as years with Niño3.4 index (ONI) in excess of plus (minus) one standard deviation (Shaman and Tziperman, 2011; Vashisht *et al*., 2021) for the 2-month average of the period of interest (JA or SO), where ONI is defined using SST averaged over the Niño3.4 region (5°S–5°N, 120°–170 W). Atmospheric fields used to study ENSO teleconnections to the uBN are drawn from NCEP-NCAR reanalysis records. From this record the spatial coverage of 2.5° latitude × 2.5° longitude global gridded monthly zonal and meridional wind fields from the year between 1950 and 2005 were used. This period is chosen to align with the latter half of the historical simulations in CMIP5. We choose not to include the full historical simulation on account of non-stationarity in the character of tropical climate variability between the first and second halves of the 20th century (e.g., Nicholson, 1995). Additionally, the Ethiopian meteorological network was not established until the 1950s, and there were very few meteorological stations in the country to inform gridded precipitation reconstructions prior to this decade (Funk *et al*., 2015a; 2015b).

2.3 | CMIP data and processing

The model data come from six different CMIP5 and CMIP6 (Taylor *et al*., 2012; Eyring *et al*., 2016) coupled GCMs (Table 1). These six models were selected because they have been found, in their CMIP5 version, to simulate nonlinear ocean–atmosphere coupling as well as rainfall in the eastern Pacific correctly (Cai *et al*., 2014). Each had also shown some ability to capture observed teleconnections between ENSO and East Africa (Bhattacharjee and Zaitchik, 2015; Siam and Eltahir, 2017; Vashisht *et al*., 2021), and had historical simulations from the same model lineage available in both CMIP5 and CMIP6 archives at the time we conducted this analysis. Monthly precipitation output fields from these experiments are used and only the first member of the ensemble simulations is utilized in order to provide consistent statistics across models. The monthly outputs used are SST, precipitation, geopotential height, and zonal and meridional winds. Models used in this study for CMIP5 are CanESM2, MPI-ESM-MR, MRI-CGCM3, MIROC-ESM, GISS-ES-R, IPSL-CM5A-LR and for CMIP6 are CanESM5, MPI-ESM1-2-LR, MRI-ESM2-0, MIROC6, GISS-E2-1-G, and IPSL-CM6A-LR. For each simulation, uBN precipitation was extracted using the same box as defined for observations. El Niño and La Niña events were defined using 2-month averaged Niño3.4 anomalies from model SST fields, following the

TABLE 1 Basic information about the selected coupled GCMs and their historical experiment in this study

Model ID		Modelling centre	Atmospheric resolution (lat × lon, number of layers)
1	CanESM2	Canada	2.8° × 2.8°, L35
2	MPI-ESM-MR	Germany	1.875° × ~1.9°, L95
3	MRI-CGCM3	Japan	1.125° × ~1.1°, L48
4	MIROC-ESM	Japan	~2.8° × 2.8°, L80
5	GISS-ES-R	USA	2.5° × 2°, L40
6	IPSL-CM5A-LR	France	3.75° × ~1.9°, L39
7	CanESM5	Canada	2.8125° × ~2.8°, L49
8	MPI-ESM1-2-LR	Germany	1.875° × ~2°, L47
9	MRI-ESM2-0	Japan	1.125° × ~1.1°, L80
10	MIROC6	Japan	~1.4° × 1.4°, L81
11	GISS-E2-1-G	USA	2.5° × 2°, L40
12	IPSL-CM6A-LR	France	2.5° × ~1.3°, L79

Note: Model IDs 1-6 are from CMIP5 and 7-12 from CMIP6.

same method as used for observations. The model years identified as El Niño and La Niña for each simulation are listed in Table 2.

3 | RESULTS AND DISCUSSION

3.1 | Rainfall climatology in the Upper Blue Nile sub-basin

Figures 2 and 3 show historical uBN precipitation climatology in the peak rainy season (JA) and end of rainy season (SO) using both CMIP5 and CMIP6 versions of the six selected GCMs, as well as CenTrends observation of JA rainfall (Figures 2b and 3b). Most models capture the general spatial character of JA rainfall peak successfully placing the highest rainfall totals in the western highlands of Ethiopia (though IPSL-CM5A-LR has a slight southeasterly bias in the precipitation peak). The total magnitude of precipitation, however, varies dramatically across models, with MIROC5 exhibiting a precipitation peak of over 750 mm while the GISS ES-1-G maximum barely exceeds 175 mm. Comparing CMIP6 to CMIP5, it is clear that the difference between models far exceeds the difference between CMIP generations. IPSL-CM5A shows the most obvious improvement, as the spatial character and magnitude of JA precipitation more closely matches observation in the CMIP6 version of the model. The MIROC5 wet bias is reduced in MIROC6, and the MRI-CGCM3 dry bias is reduced in MRI-ESM2. Other models show small changes in the spatial structure and magnitude of precipitation in their CMIP6 iteration, but with no clear improvement relative to observation. When results are broken down by month (July and August) the results are generally similar (Figures S1 and S2).

Looking at the historical precipitation climatology during SO, there are some similarities to the patterns identified for JA. Again, MIROC5 has a wet bias that is somewhat reduced in MIROC6, and the GISS models are again the driest of this ensemble. Interestingly, a southward bias in the precipitation maximum found in MRI-CGCM3 is improved in MRI-ESM2, indicating that the CMIP6 version of this model has improved representation of intertropical convergence zone (ITCZ) migration in this portion of East Africa. The tendency is evident in both September and October (Figures S3 and S4). GISS-ES-G-1, though dry relative to observations, shows improved magnitude and spatial distribution of SO precipitation compared to GISS-ES-R in the CMIP5 ensemble. This includes capturing the general character of the southeasterly progression in the precipitation maximum from September to October.

3.2 | Associations of ENSO with uBN precipitation

Though mean statistics of precipitation are commonly invoked as measures of GCM performance, the ability of models to capture large-scale drivers of precipitation variability is arguably more important (Bhattacharjee and Zaitchik, 2015). Mean precipitation can, when necessary, be adjusted through bias correction procedures. Ability to capture critical teleconnections, however, is less easily addressed on a nonstationary climate background, so projections are more likely to rely on the GCM to capture these relationships over time.

For this region, ENSO is a leading driver of interannual precipitation, as most major droughts in the uBN have come under El Niño conditions. This association is evident in the strong negative correlations between the Niño3.4 index and precipitation across the uBN in JA (Tables 3 and 4). The representation of this teleconnection is inconsistent across models. The GISS and IPSL models capture the character of the negative association in both CMIP5 and CMIP6, while MIROC and MRI models show only a weak negative correlation in CMIP5 and actually degrade to a slight positive correlation in CMIP6. The greatest improvement between CMIP5 and CMIP6 is seen in CanESM and, to a lesser degree, MPI-ESM, which both show strengthened negative correlation in CMIP6 relative to CMIP5. Overall, the ensemble of the six model realizations does capture a negative association between Niño3.4 and uBN precipitation in both CMIP5 and CMIP6, with a negligible strengthening of that negative association between CMIP5 and CMIP6.

It is instructive to consider the spatial distribution of these correlations across the uBN and surrounding areas. Observations indicate a clear divide between a northwest region of negative correlation that includes the uBN highlands and a southeast region that has positive correlations (Figure 4). This spatial distribution is evident in a general sense (allowing for GCM imprecision at local scales) in GISS and MIROC models, and to a lesser extent in MRI and MPI models. IPSL does not include the southeastern region of positive correlation, and CanESM correlation patterns bear little resemblance to observations. This result suggests that models like MIROC6 might offer meaningful simulation of the ENSO teleconnection if spatial biases could be accounted for, as the region of negative correlation simply seems to be displaced from the uBN. And while CanESM5 captures the spatially averaged correlation quite convincingly (Table 4), the odd spatial character of the correlation results encourages further investigation.

The issue of ENSO correlation becomes more complicated in SO. Though we group these months because they

TABLE 2 ENSO years for JA seasons of each model for simulation period 1950–2005

	El Niño years		La Niña years	
Model	**JA**	**SO**	**JA**	**SO**
CMIP5				
CanESM2	1955, 1961, 1965, 1973, 1977, 1981, 2005	1961, 1973, 1977, 1981, 2005	1974, 1978, 1983, 1986, 1997	1974, 1978, 1986, 1997
GISS-ES-R	1962, 1973, 1977, 1979, 1989, 1998	1962, 1967, 1973, 1977, 1979, 1981, 1985, 1989, 1992, 1998, 2000	1963, 1966, 1984, 1991, 1993, 1996	1963, 1966, 1971, 1993, 1996
IPSL-CM5A-LR	1953, 1960, 1963, 1967, 1982, 1993, 1997, 1999, 2000	1959, 1960, 1963, 1969, 1981, 1989, 1993, 1997, 2000, 2003	1958, 1978, 1980, 1985, 1994, 1998	1978, 1984, 1985, 1994
MIROC-ESM	1952, 1960, 1965, 1975, 1992, 1993, 2003, 2004	1959, 1960, 1965, 1975, 1986, 1992, 2003, 2004	1953, 1962, 1967, 1977, 1988, 1994	1967, 1977, 1988, 1994
MPI-ESM-MR	1961, 1974, 1975, 1996, 1999, 2000	1961, 1967, 1974, 1996, 1999, 2000	1964, 1979, 1982, 1994, 2002	1959, 1963, 1964, 1979, 1981, 1982, 2002
MRI-CGCM3	1960, 1963, 1968, 1975, 1977, 1984, 1988, 1991, 2004	1954, 1960, 1963, 1968, 1975, 1977, 1984, 2004	1973, 1985, 1986	1973, 1985, 1986, 2005
CMIP6				
CanESM5	1950, 1965, 1970, 1971, 1985, 1989, 1991, 1992, 2001, 2004	1968, 1970, 1977, 1985, 1989, 1991, 1992, 2001	1966, 1967, 1975, 1978, 1996, 2003, 2005	1963, 1966, 1975, 1996
GISS-E2-1-G	1960, 1964, 1980, 1984, 1993, 1997, 2001	1951, 1960, 1964, 1972, 1976, 1980, 1984, 1993, 1996, 1997, 2001	1962, 1966, 1970, 1982, 2003	1962, 1966, 1970, 1982, 1998, 2003
IPSL-CM6A-LR	1957, 1965, 1971, 1976, 1983, 1988, 1996, 2000	1965, 1971, 1976, 1983, 1988, 1996, 2000	1961, 1977, 1980, 1989, 1998	1953, 1961, 1980, 1989, 1998
MIROC6	1953, 1962, 1969, 1976, 1983, 1991	1961, 1962, 1969, 1976, 1982, 1983, 1991	1950, 1963, 1964, 1985, 1987, 1993	1963, 1964, 1985, 1992, 1993
MPI-ESM1-2-LR	1960, 1980, 1985, 1991, 1992, 1996, 2003	1960, 1967, 1973, 1985, 1992, 1996, 2003	1963, 1975, 1988, 1994, 1999	1963, 1975, 1994
MRI-ESM2-0	1970, 1974, 1978, 1985, 1987, 1990, 2000, 2005	1970, 1974, 1978, 1985, 1987, 1990, 2000, 2004, 2005	1975, 1977, 1986, 2002	1975, 1977, 1979, 1983, 1986, 2002

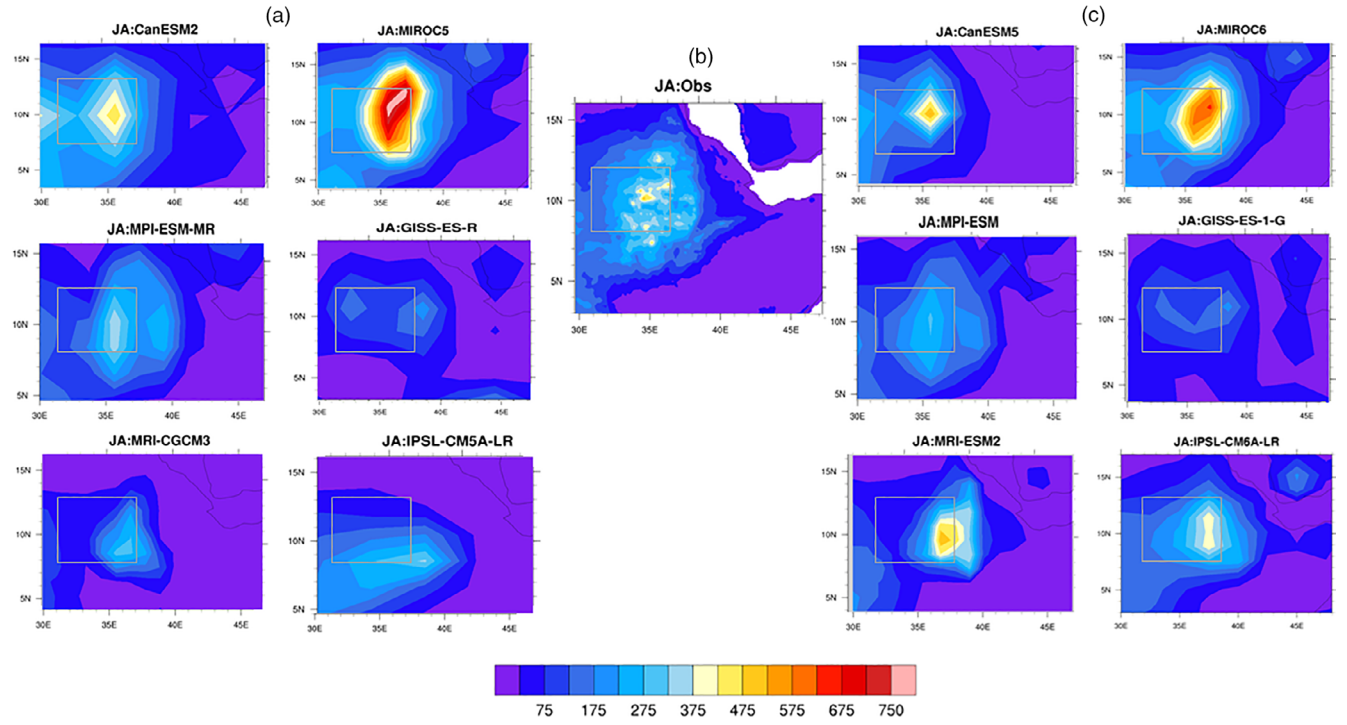

FIGURE 2 Historical JA precipitation climatology (mm·year^{-1}) over uBN using (a) CMIP5 models, (b) CenTrends, and (c) CMIP6 models

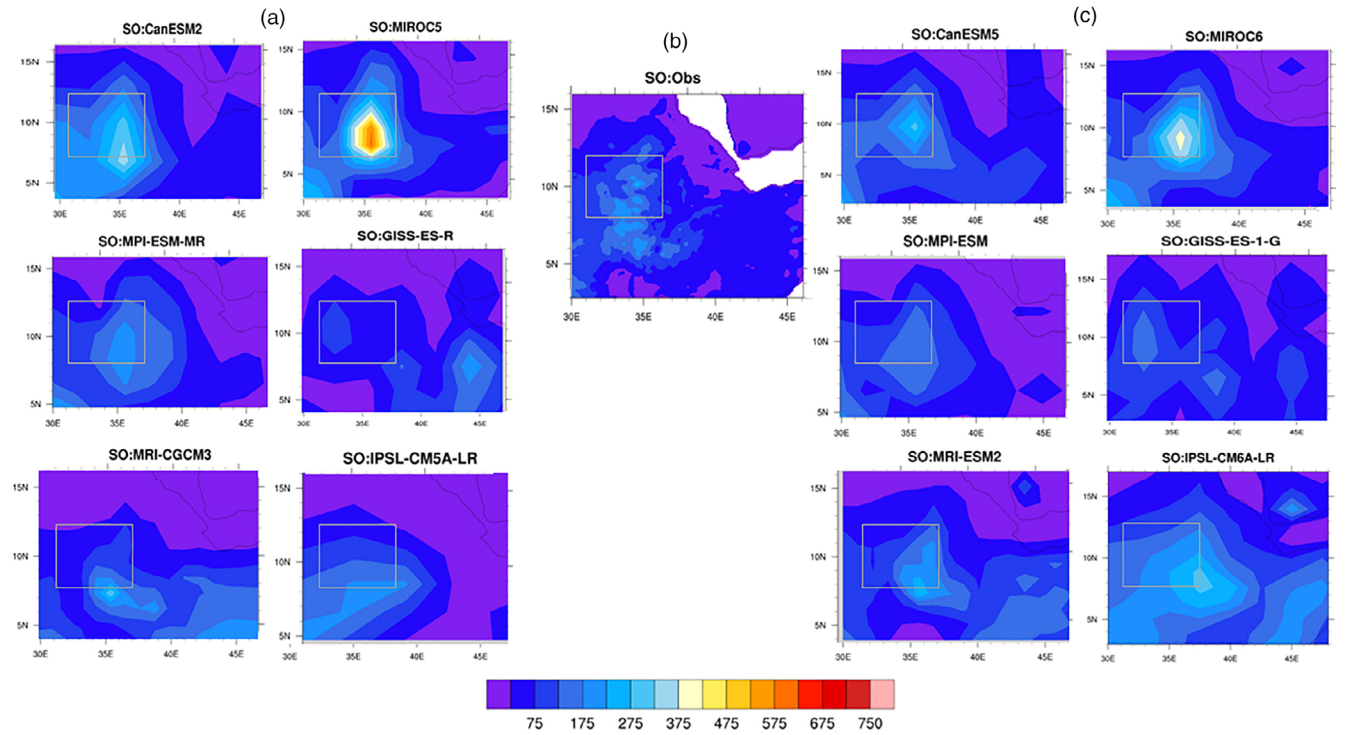

FIGURE 3 Historical SO (end of rainy season) precipitation climatology (mm·year^{-1}) over uBN in (a) CMIP5 models, (b) CenTrends, and (c) CMIP6 models

represent the end of the rainy season in the uBN—the month of cessation can differ from year to year or across locations within the uBN—the months are transitional in that they capture the recession of the ITCZ and a gradual shift in the nature of ENSO projection onto the region. Whereas negative correlations between ENSO and

TABLE 3 Correlations of Niño3.4 SST with uBN precipitation (CMIP5)

Model	JA	SO	Sep	Oct
CenTrends	**−0.72**	−0.13	−0.23	**0.45**
CanESM2	−0.06	0.13	−0.01	**0.34**
GISS5-ES-R	**−0.41**	**−0.35**	**−0.54**	0.01
MIROC5	−0.10	**−0.30**	**−0.55**	0.14
IPSL-CM5A-LR	**−0.51**	−0.01	**−0.29**	**0.32**
MPI-ESM-MR	−0.01	−0.11	**−0.28**	0.10
MRI-CGCM3	−0.22	−0.14	−0.25	0.06
Ensemble	−0.22	−0.13	−0.32	0.16

Note: Bold font indicates significance for a 2-tailed test at $p < .05$ for 1950–2005.

TABLE 4 Correlations of Niño3.4 SST with uBN precipitation (CMIP6)

Model	JA	SO	Sep	Oct
CenTrends	**−0.72**	−0.13	−0.23	**0.45**
CanESM5	**−0.45**	−0.18	−0.24	−0.01
GISS-ES-1-G	**−0.51**	−0.15	**−0.41**	0.13
MIROC6	0.12	−0.01	**−0.36**	**0.36**
IPSL-CM6A-LR	**−0.51**	−0.22	−0.24	−0.15
MPI-ESM	−0.22	−0.12	−0.25	0.01
MRI-ESM2	0.02	**0.37**	−0.17	**0.50**
Ensemble	−0.26	−0.05	−0.28	0.14

Note: Bold font indicates significance for a 2-tailed test at $p < 0.05$ for 1950–2005.

rainfall are generally understood to dominate in JA, boreal autumn sees the onset of the "short rains" in equatorial East Africa, in which there are generally positive correlations between ENSO and rainfall. SO, then, falls in a time of shifting teleconnection sign and mechanism. Recognizing this transitional nature, we look at SO as a combined 2-month "end of rainy season" period and also examine each month separately.

As shown in Tables 3 and 4, the shifting teleconnection is captured in observations as a shift from strong negative correlation in September to nonsignificant, slightly negative correlation in October. Taken together there is significant negative correlation in SO, but it is approximately half as strong as the correlation seen for JA. The general pattern of waning correlations from September to October is captured in the ensemble average of both CMIP5 and CMIP6. Indeed, all simulations considered in this study for both CMIP5 and CMIP6 show a more strongly negative correlation in September than in October. All but two models capture the overall negative sign of correlation for SO (the exceptions are CanESM2 in CMIP5 and MRI-ESM2 in CMIP6). Comparing the CMIP6 ensemble to the CMIP5 ensemble, there is a general weakening in the strength of September correlations that drives the ensemble away from observations. October results are difficult to characterize, as there is a wide spread between models and there is little consistency within model families between CMIP5 and CMIP6. Overall, it appears that the timing of the shift in ENSO teleconnections between boreal summer and boreal fall is a difficult dynamic for models to capture in a consistent way. This has considerable implications for projections of future climate impacts in the uBN, where the end of the rainy season is critical for a number of agricultural activities (Zeleke *et al.*, 2017; Ademe *et al.*, 2021).

Spatially, the shift in correlation pattern from JA to SO is evident as a strengthening and extension of the zone of positive ENSO correlation to the southeast of the uBN and a patchwork of correlations in the uBN itself (Figure 5). It is difficult to see evidence of this spatial pattern in the CMIP models. There is some indication of an east–west correlation split in some models, and MPI-ESM and CanESM5, both in the CMIP6 ensemble, show perhaps the closest resemblance to the spatial distribution of correlations seen in observations, but the resemblance is not strong. This lack of spatial coherence is further indication that GCMs struggle to capture the end-of-rains transition in ENSO influence.

It is important to keep in mind that these ENSO correlation results are for a reasonably modest number of events, and that we are considering only univariate correlations in this study. As each ENSO event in the historic record or in a model realization occurs in the context of other modes of climate variability and with its own distinctive character, these results should be viewed as general indicators of model performance relative to the limited historical record. As shown in Figure 6, the uBN precipitation anomaly associated with El Niño and La Niña events differs substantially between events.

Tables 5 and 6 approach ENSO-related precipitation anomalies probabilistically, considering the percentage of events that show the expected anomaly. In the CenTrends record, we see that there has been a 68.4% alignment between JA El Niño events and negative precipitation anomalies, but for SO and for JA La Niña there are counterexamples to the standard narrative that El Niño brings drought and La Niña brings above average precipitation to the uBN. In the CMIP5 and CMIP6 ensembles, MRI-CGCM3 and MRI-ESM2 stand out as being particularly unlikely to simulate negative

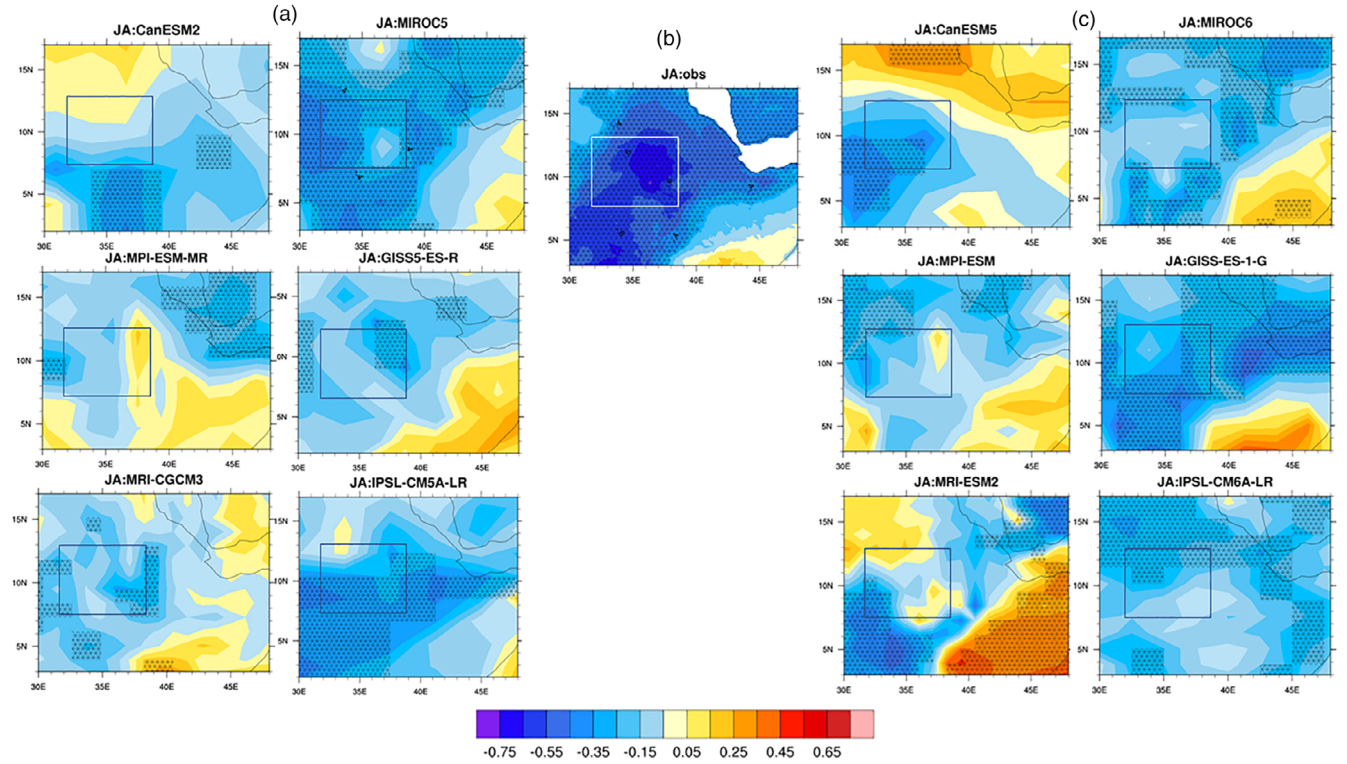

FIGURE 4 Historical JA (beginning of rainy season) precipitation correlations of uBN with Niño3.4 regions in (a) CMIP5 models, (b) CenTrends, and (c) CMIP6 models. Correlations are calculated for 1950–2005 in CenTrends and 1950–2005 in models. Stippling indicates statistical significance at $p < .05$

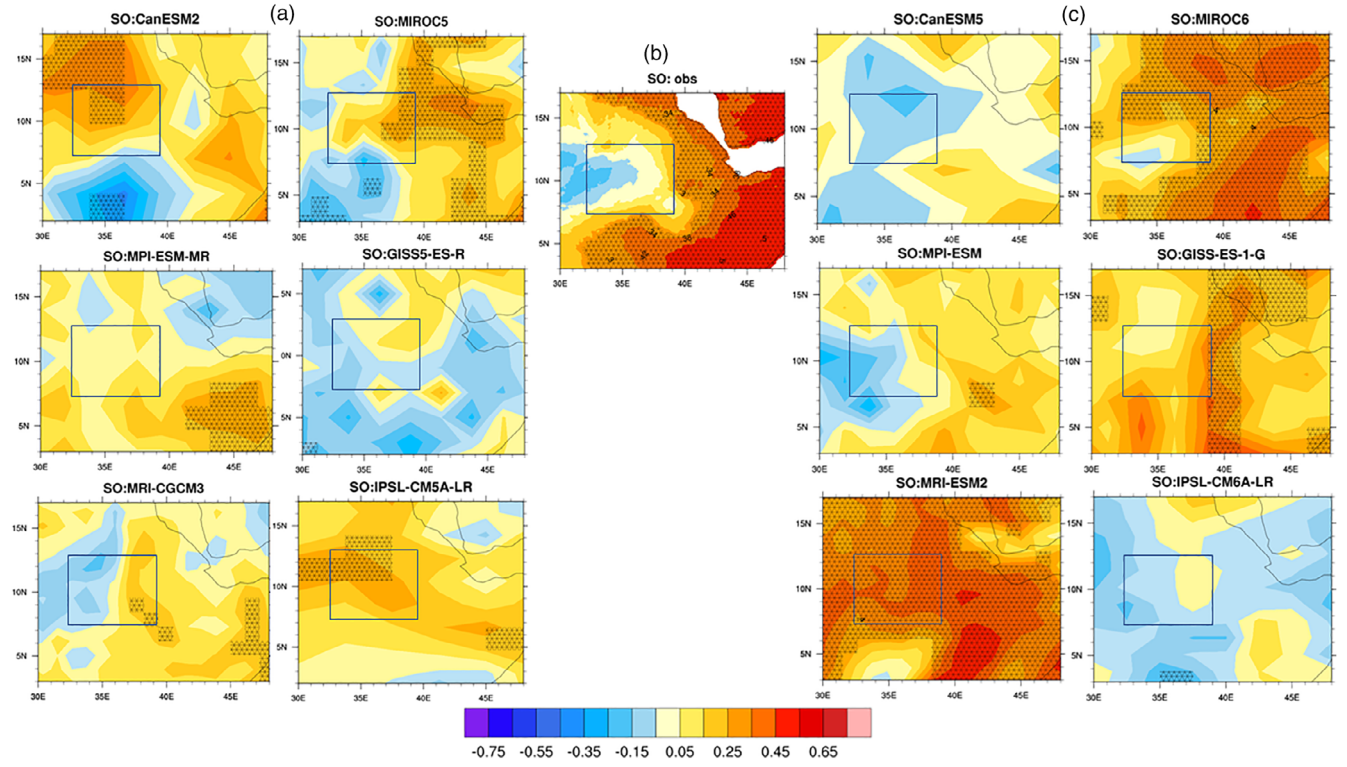

FIGURE 5 Historical SO (end of rainy season) precipitation correlations of uBN with Niño3.4 regions in (a) CMIP5 models, (b) CenTrends, and (c) CMIP6 models. Correlations are calculated for 1950–2005 in CenTrends and 1950–2005 in models. Stippling indicates statistical significance at $p < .05$

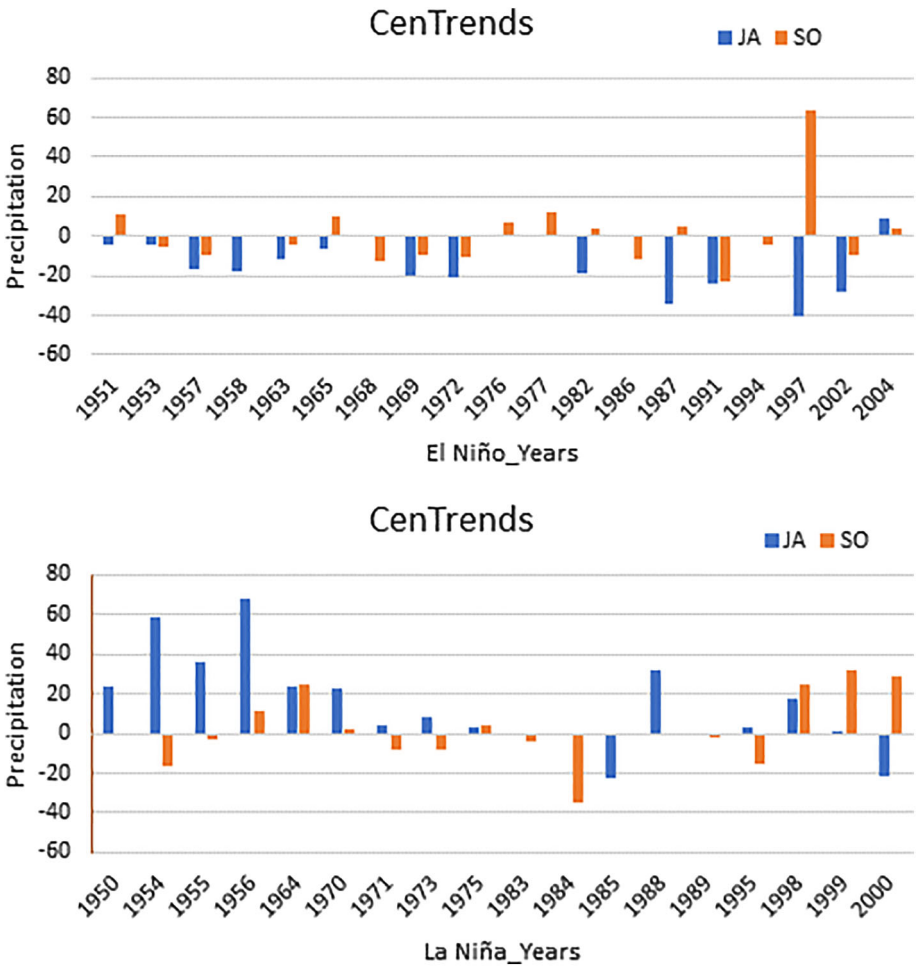

FIGURE 6 uBN precipitation anomalies (mm) for El Niño and La Niña events during the 1950–2005 baseline observational period. Years with only a single bar result from ENSO events that were present only in JA or SO

TABLE 5 Percentages of El Niño/La Niña events showing the expected precipitation anomaly (mm), and the average precipitation anomaly for those events, for JA and SO of CMIP5

	El Niño				La Niña			
	JA		SO		JA		SO	
Model name	% neg. anom. events	Mean. pre. anom.	% neg. anom events	Mean. pre. anom.	% pos. anom events	Mean. pre. anom.	% pos. anom. events	Mean. pre. anom.
CenTrends	68.4	−3.2	52.6	1.4	72.2	7.7	38.9	10.8
CanESM2	83.3	−81.0	40.0	34.0	0.0	−65.1	0.0	−46.1
MPI-ESM-MR	66.7	−14.0	33.3	4.7	60.0	8.1	83.3	18.8
MRI-CGCM3	55.6	−4.1	57.1	−7.1	66.7	10.1	25.0	−13.4
MIROC5	71.4	−16.5	57.2	−6.3	100.0	47.9	50.0	5.2
GISS-ES-R	83.3	−12.9	54.6	0.0	83.3	11.7	60.0	0.7
IPSL-CM5A-LR	87.5	−64.8	44.4	4.2	80.0	57.9	25.0	−14.9

Note: Anomalies are calculated as the average JA (SO) precipitation total in El Niño or La Niña years minus the climatological mean JA (SO) precipitation. for 1950–2005.

anomalies during JA El Niño events, relative both to observations and to other models. For SO, MIROC6 and MRI-ESM2 are the least likely to capture low precipitation associated with El Niño. For La Niña, CMIP models are relatively consistent in simulating positive precipitation anomalies in JA—especially in the CMIP6

TABLE 6 Percentages of El Niño/La Niña events showing the expected precipitation anomaly (mm), and the average precipitation anomaly for those events, for JA and SO of CMIP6

	El Niño				La Niña			
	JA		SO		JA		SO	
Model name	% neg. anom. events	Mean. pre. anom.	% neg. anom. events	Mean. pre. anom.	% pos. anom. events	Mean. pre. anom.	% pos. anom. events	Mean. pre. anom.
CenTrends	68.4	−3.2	52.6	1.4	72.2	7.7	38.9	10.8
CanESM5	87.5	−53.0	75.0	−16.6	71.4	71.1	75.0	20.0
MPI-ESM	100	−22.7	42.9	−2.0	60.0	6.1	66.7	1.7
MRI-ESM2	50.0	−2.9	22.2	41.1	50.0	8.2	0.0	−39.3
MIROC6	80.0	−12.2	28.6	8.5	80.0	16.5	40.0	−7.0
GISS-ES-1-G	85.7	−24.9	50.0	4.6	80.0	33.6	33.3	−3.8
IPSL-CM6A-LR	57.1	−0.7	57.1	−4.1	80.0	17.1	25.0	−7.9

Note: Anomalies are calculated as the average JA (SO) precipitation total in El Niño or La Niña years minus the climatological mean JA (SO) precipitation for 1950–2005.

ensemble—while results for SO are inconsistent in both the CMIP5 and CMIP6 ensembles.

4 | MECHANISM

4.1 | Climatology of TEJ

The mechanisms through which ENSO influences boreal summer uBN precipitation are still a topic of research (Vashisht *et al*., 2021). One leading hypothesis is that ENSO modulates divergence in the exit region of the TEJ (Hastenrath, 1991; Grist and Nicholson, 2001; Diro *et al*., 2011). The TEJ is weaker under El Niño conditions, which can have the effect of reducing exit region divergence over the Ethiopian Highlands, thus inhibiting deep convection (Gleixner *et al*., 2017). Working from this hypothesis, and building on previous work on TEJ relationships with uBN rainfall in the CMIP5 ensemble (Vashisht *et al*., 2021), we examine associations between ENSO state, TEJ activity, and uBN precipitation in our ensemble of selected CMIP5 and CMIP6 GCMs.

First, we consider model representation of the basic features of the TEJ in JA and SO. The TEJ is a dominant feature in the upper troposphere across tropical Asia and Africa in boreal summer. It is characterized by strong easterly mean flow, though it includes frequent meanders to the north or south. It reaches peak velocity in June–September, with a wind speed maximum located over the central and western Indian Oceans at a height of ∼150 mb (Flohn, 1964). The jet extends from Southeast Asia to Africa, where it gradually weakens from east to west (Figure 7b). Meridionally, easterly flow associated with the jet occurs in the zone 5°–20°N (Wang *et al*., 2005), the mean axis of maximum winds being located between 5°N and 15°N, perhaps slightly closer to the equator over Africa than in the entrance region over Southeast Asia. Its intensity shows a strong relationship to the intensity of the Indian monsoon, with a stronger (weaker) jet associated with anomalously high (low) monsoon rainfall (Pattanaik and Satyan, 2000; Nicholson and Klotter, 2021). Detailed knowledge about the jet stream's location, altitude, and strength is a key factor for weather and climate forecasts in the South Asian monsoon region (Rao and Srinivasan, 2016). The TEJ fades in strength and shifts southeast at the end of boreal summer, with average windspeeds on the order of 20–25 $m \cdot s^{-1}$ in the core of the jet (Figure 8b).

All GCMs in our selected CMIP5 and CMIP6 ensemble contain a wind feature that resembles the TEJ, indicating that the models are able to capture the large-scale thermal wind relation between the tropical Indian Ocean and the Tibetan Plateau. The character of this feature, however, differs dramatically across models. Among CMIP5 GCM's (Figure 7a), MPI-ESM-MR and, to some extent, MIROC5 and IPSL-CM5A-LR capture the maximum intensity feature of the JA TEJ core, while CanESM2 underestimates intensity and GISS-ES-R and IPSL-CM5A-LR have a weak JA TEJ that is displaced eastward relative to observations. In CMIP6 (Figure 7c), CanESM5 shows improved representation of TEJ core strength, while MPI-ESM and MIROC6 maintain their CMIP5 performance. IPSL-CM6A-LR captures the spatial character of the TEJ but wind speeds are weak relative to observation and to the CMIP5 version of the model. Insomuch as TEJ strength is important to uBN precipitation processes

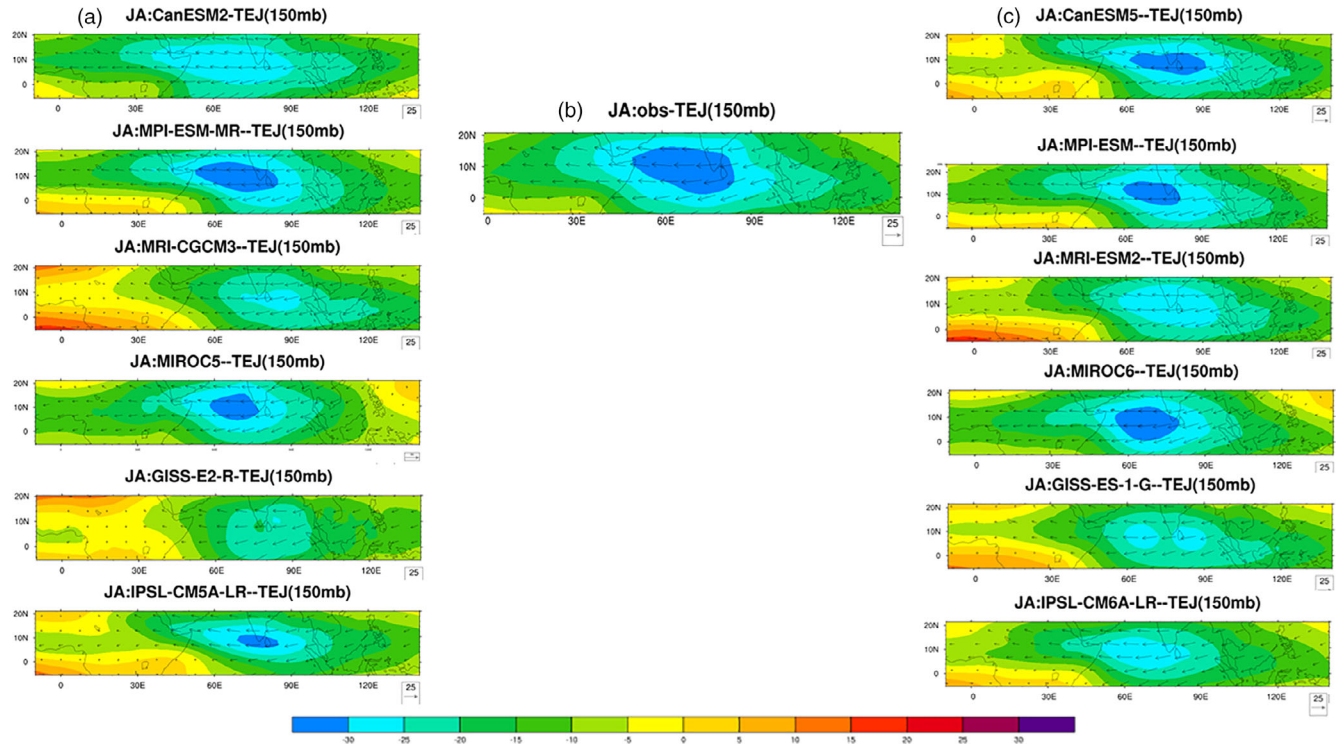

FIGURE 7 TEJ climatological JA zonal wind ($m \cdot s^{-1}$) at 150 mb in (a) CMIP5 models, (b) reanalysis, and (c) CMIP6 models. Colours shows zonal wind magnitudes

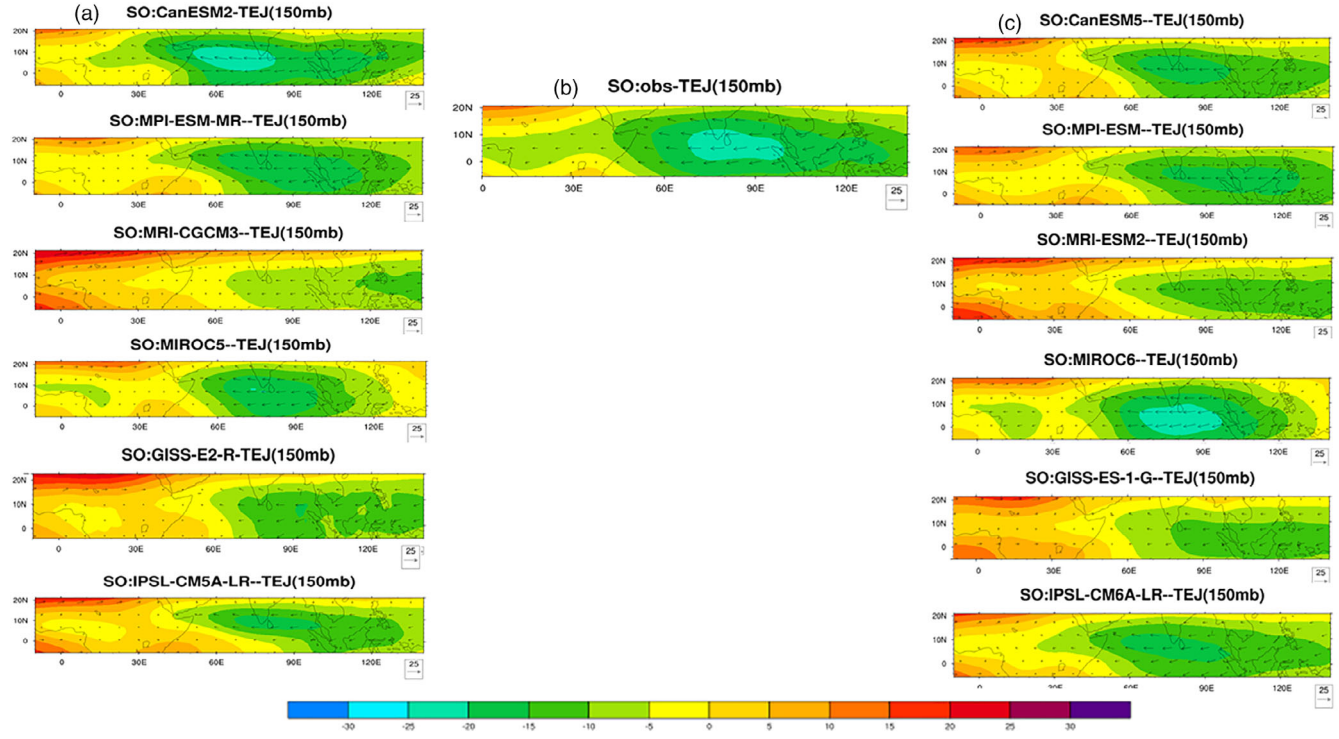

FIGURE 8 TEJ climatological SO (end of rainy season) zonal wind (m/s) at 150mb for (a) CMIP5 models, (b) reanalysis, and (c) CMIP6 models. Colours show zonal wind magnitudes

and to the ENSO teleconnection to the region, a model's ability to capture these general features of the JA TEJ could be important for its reliability in the region.

In SO, there is a general tendency for GCMs to underestimate the strength and westward influence of the TEJ. This tendency persists from CMIP5 to CMIP6 models. CanESM2 is one exception, as it exhibits a fairly strong SO TEJ that falls somewhat west of observations (Figure 8a). MIROC6 offers one example of a GCM that has improved representation of TEJ position (Figure 8c), strength, and westward influence relative to the CMIP5 version of the model. All other models show a general windspeed maximum that extends into the central Indian Ocean sector, but the feature is weak and is often an extension of a wind speed peak over Southeast Asia that extends to the Indian Ocean, rather than appearing as a local maximum in its own right. Interestingly, if September is considered alone then the picture is somewhat better, with multiple CMIP5 and CMIP6 GCMs capturing the approximate location of the TEJ windspeed maximum (Figure S5), though with no systematic change between CMIP5 and CMIP6. The weak and displaced TEJ in SO, then, is largely a function of models' simulating a too-rapid decay of TEJ strength into October (Figure S6).

The representation of TEJ strength across all models and for both JA and SO is summarized in Figure 9. The diversity of TEJ representation between models is evident in both the CMIP5 and CMIP6 ensembles. Notably, however, the ensemble means of these six GCMs more closely resembles observation in CMIP6 than in CMIP5, both in terms of the longitude of the TEJ peak and the absolute wind speeds in the TEJ core and to its west. No such systematic improvement is seen for the SO season.

4.2 | ENSO–TEJ associations

The variability of the tropical easterly wind speed in the upper troposphere depends on the meridional temperature gradient between the tropical Indian Ocean and subtropical Asia, and it is also sensitive to influence from the large-scale tropical atmospheric circulation. Joseph and Sabin (2008) related the weakening of TEJ associated with increased warming over the Indian Ocean and thus higher sea surface temperature (SST) along with convection. Chen and van Loon (1987) showed that TEJ speed is also sensitive to changes in divergence associated with atmospheric circulation patterns. These sensitivities indicate a potential relationship between ENSO state and TEJ strength, and past studies have shown a negative association between Niño3.4 SSTs and TEJ strength.

In Figures 10 and 11 we examine spatial correlation patterns between 150 hPa zonal wind speed and Niño3.4

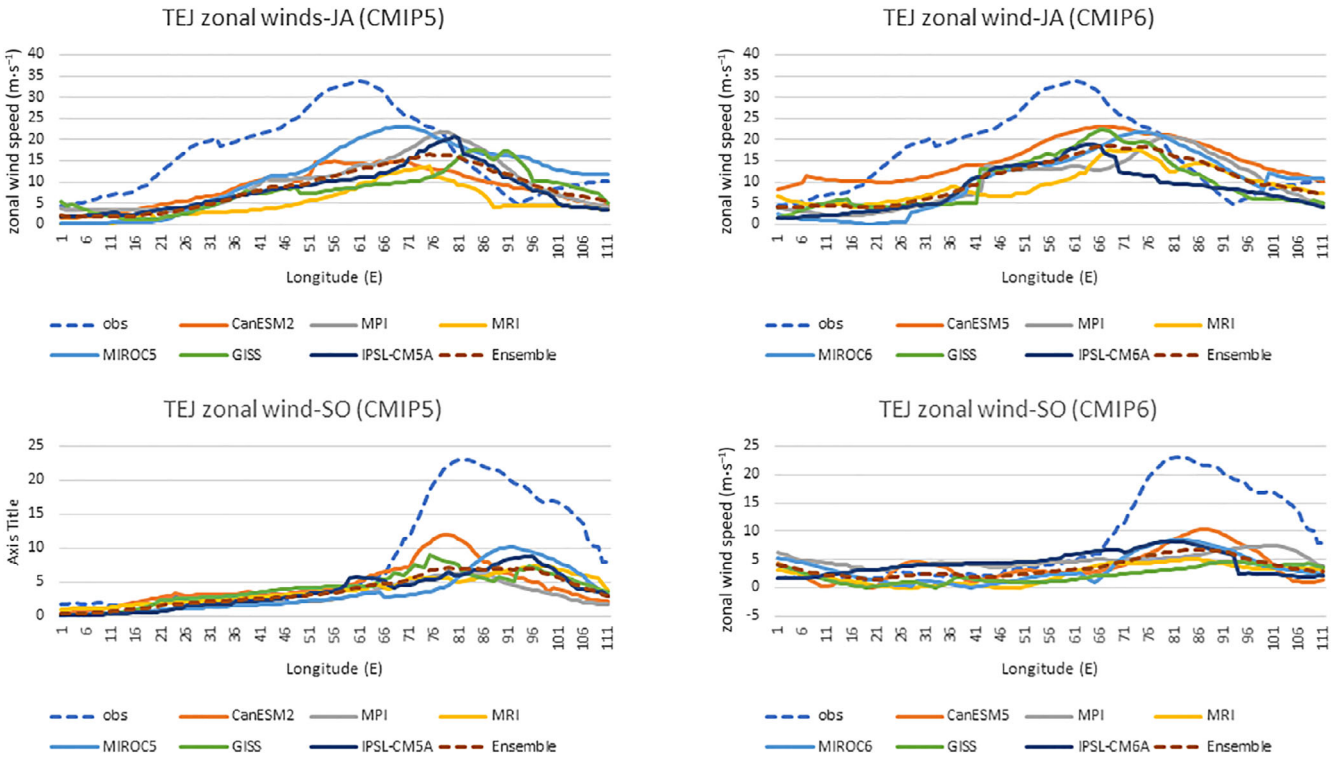

FIGURE 9 Longitudinal line plot of TEJ climatology (averaged over 2°–12°N, easterlies considered positive) using observations, CMIP5 and CMIP6 GCMs

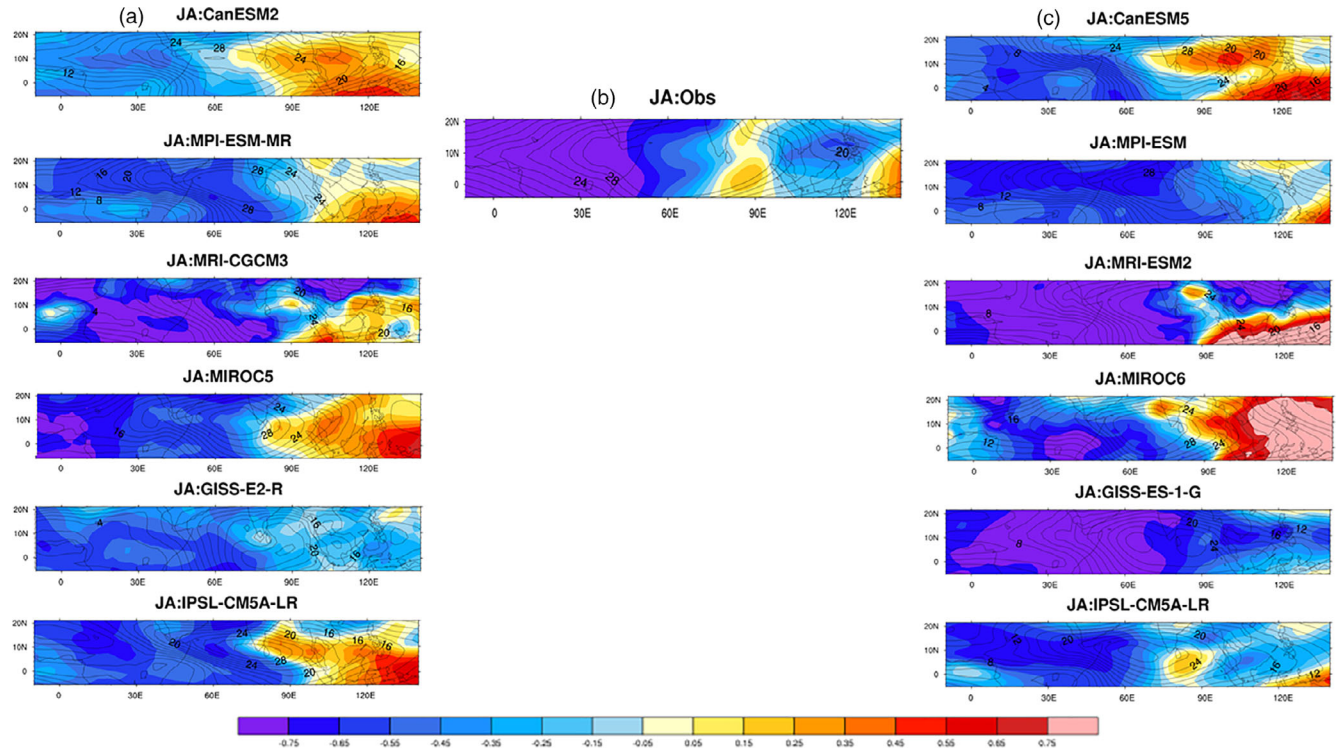

FIGURE 10 Correlation (based on absolute wind speed) between ENSO and TEJ in JA (beginning of rainy season) of (a) CMIP5 models, (b) reanalysis, and (c) CMIP6 models. Contour lines indicate wind speed. Correlation coefficients with absolute value >0.264 are statistically significant at $p < 0.05$

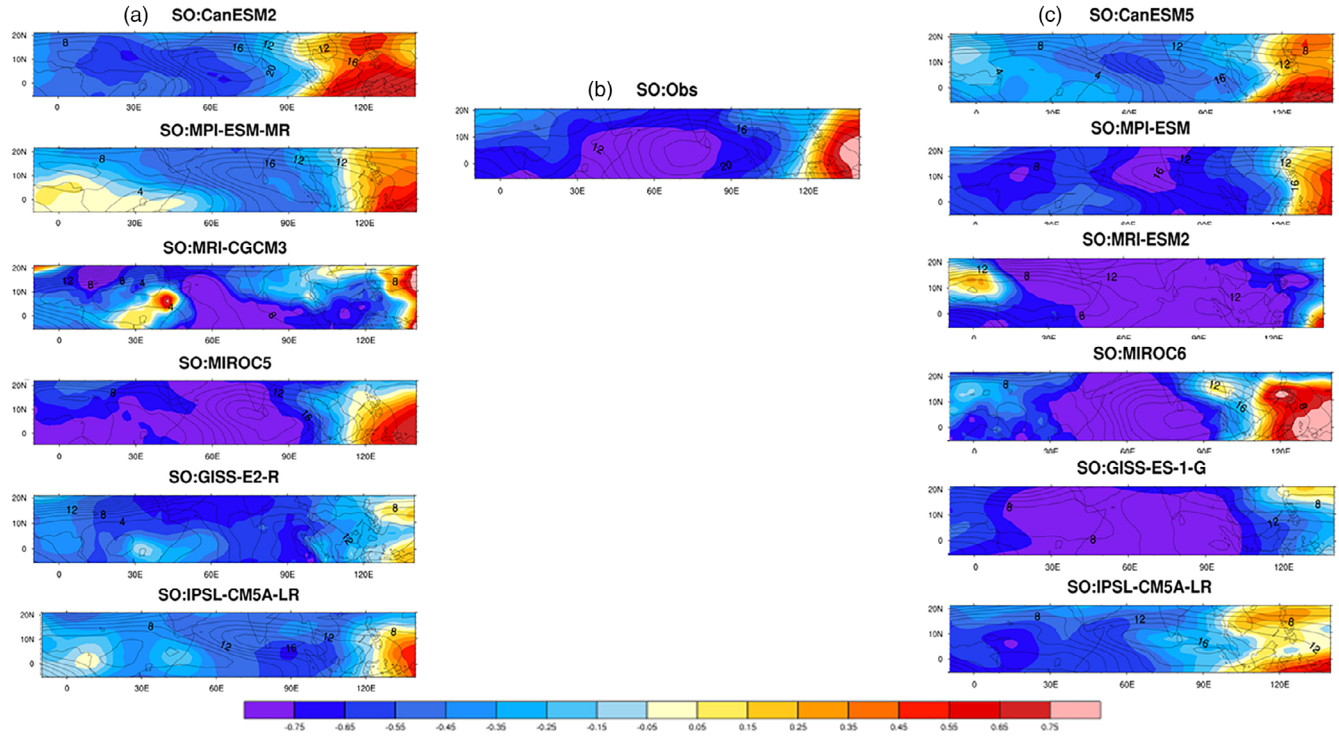

FIGURE 11 Correlation (based on absolute wind speed) between ENSO and TEJ in SO (end of rainy season) for (a) CMIP5 models, (b) observation, and (c) CMIP6 models. Contour lines indicate wind speed. Correlation coefficients with absolute value >0.264 are statistically significant at $p < .05$

in JA and SO. For JA (Figure 10) Correlations are negative in the core TEJ region and in the westward jet exit region, including over the uBN, in both observation and models. This general similarity indicates that CMIP5 and CMIP6 GCMs are able to capture the basic large-scale relationship between ENSO and TEJ speed, including the tendency for reduced speeds and hence reduced divergence in the jet exit region during El Niño, which is hypothesized to be a mechanism for ENSO influence on the uBN summer rains. Models differ in the extent and strength of the negative association between Niño3.4 and 150 hPa zonal wind speeds, with CanESM2 showing relatively weak associations and GISS-ES-1-G and MRI-ESM2 showing particularly strong negative correlations that extend to the eastern Indian Ocean.

In general, CMIP6 models have stronger and more extensive negative correlations than their CMIP5 counterparts, indicating stronger simulated coupling between ENSO and tropical circulations in the upper troposphere. The comparison in Figure 12 shows, strong negative correlation between Niño3.4 and TEJ wind speed in CMIP6 than CMIP5 models during both SO and JA seasons. While CanESM5 and IPSL-CM6A-LR show improved spatial agreement with observation relative to CMIP5 versions of those models, the changes in the other GCMs sometimes leads to negative correlations that are stronger and more extensive than those seen in reanalysis.

As shown above, the SO TEJ is weaker and shifted southeast relative to the JA TEJ (Figure 8). ENSO influence on zonal winds at TEJ height, however, is still strong. In this season there are negative correlations between Niño3.4 and zonal wind speed throughout the TEJ core and surrounding regions, including the jet exit region. In this season there are clearer signs of improvement between CMIP5 and CMIP6 (Figure 11a,c). With the exception of CanESM5, all CMIP6 models show signs of convergence towards observed correlation patterns relative to their CMIP5 predecessors. This includes stronger and more consistent negative correlations in the TEJ core and exit regions in MPI-ESM1-2-LR, MRI-ESM2, GISS-ES-1-G, and IPSL-CM6A-LR.

Meridionally averaged correlations between Niño3.4 and TEJ wind speed indicate that observed correlations are negative between 78°E and 0°E for JA and 60°E and 0°E in SO (Figure 12). This general pattern of positive correlations in the east and negative correlations in the west is captured by most CMIP5 and CMIP6 models. Exceptions are MRI-CGCM3 and MRI-ESM2 in SO and GISS-ES-R in JA, which show negative correlations at all longitudes.

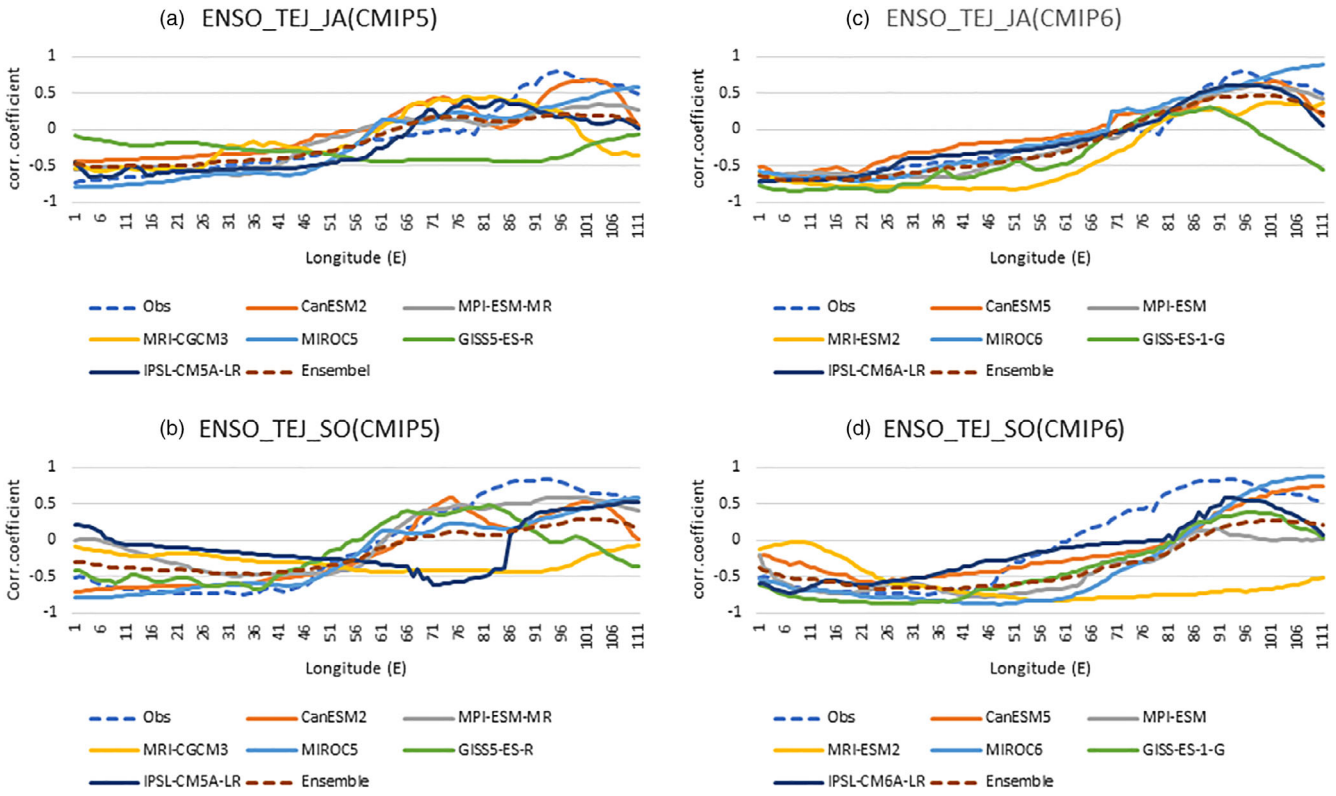

FIGURE 12 Longitudinal line plot showing Niño3.4 and TEJ wind speed (150 hPa) correlation for (a, c) JA, averaged over 5°–15°N, and (b, d) SO, averaged over 2°–12°N, for (a, b) CMIP5 and (c, d) CMIP6 models, alongside observation. All calculations are for 1950–2005. Correlation coefficients with absolute value >0.264 are statistically significant at $p < .05$ for observations and for individual models

Comparing CMIP5 to CMIP6, there is a tendency towards better agreement with JA observations in CMIP6, including a general tightening of the ensemble spread (Figure 12a,b). But for SO the CMIP6 ensemble converges on correlation patterns that are not particularly well aligned with observations (Figure 12c,d). This causes the CMIP6 ensemble mean for SO correlation patterns to fall quit far from observations, which is in contrast to the relatively good alignment between ensemble mean correlations and observed correlations in JA and, for CMIP5, in SO.

4.3 | Correlation between TEJ and uBN precipitation

Figures 13 and 14 examine associations between 150 hPa winds in the TEJ region and uBN precipitation variability in observations and models for JA and SO, respectively. Negative correlations indicate that uBN precipitation decreases with increasing wind strength, and vice versa. Consistent with previous studies, we see that in observation there are strong positive correlations between 150 hPa wind speed in the jet exit region and JA precipitation in the uBN (Figure 13b). This is consistent with the hypothesis that reduced wind speed in the jet exit region inhibits convection in the Ethiopian Highlands due to reduced divergence aloft. There is evidence of this relationship in nearly all CMIP5 and CMIP6 models included in our ensemble: spatially coherent positive correlations are found between wind speed in the jet exit region and uBN rainfall in all models except for MPI-ESM-MR and MPI-ESM1-2-LR (and, to some extent, CanESM2, which shows weaker positive correlations). Differences between CMIP5 and CMIP6 are not consistent across models. Where CanESM5 has stronger correlations than CanESM2, more closely resembling observations, MIROC6 and IPSL-CM6A-LR show weakened correlations over East Africa, making those models less similar to observations than their CMIP5 predecessors in the region most relevant to uBN rainfall.

Notably, while the observed relationships between 150 hPa wind speed and uBN precipitation are relatively stable across July and August (Figures S7 and S8), several models show volatility in correlation patterns between these months. This speaks to the noisiness of precipitation records and wind fields in model simulations and emphasizes the need for caution when applying seasonal averages to understand teleconnection mechanisms.

Figure 14 shows uBN precipitation correlations with 150 hPa wind speed for SO. In observation (Figure 14b), positive correlations are found over the extended TEJ exit

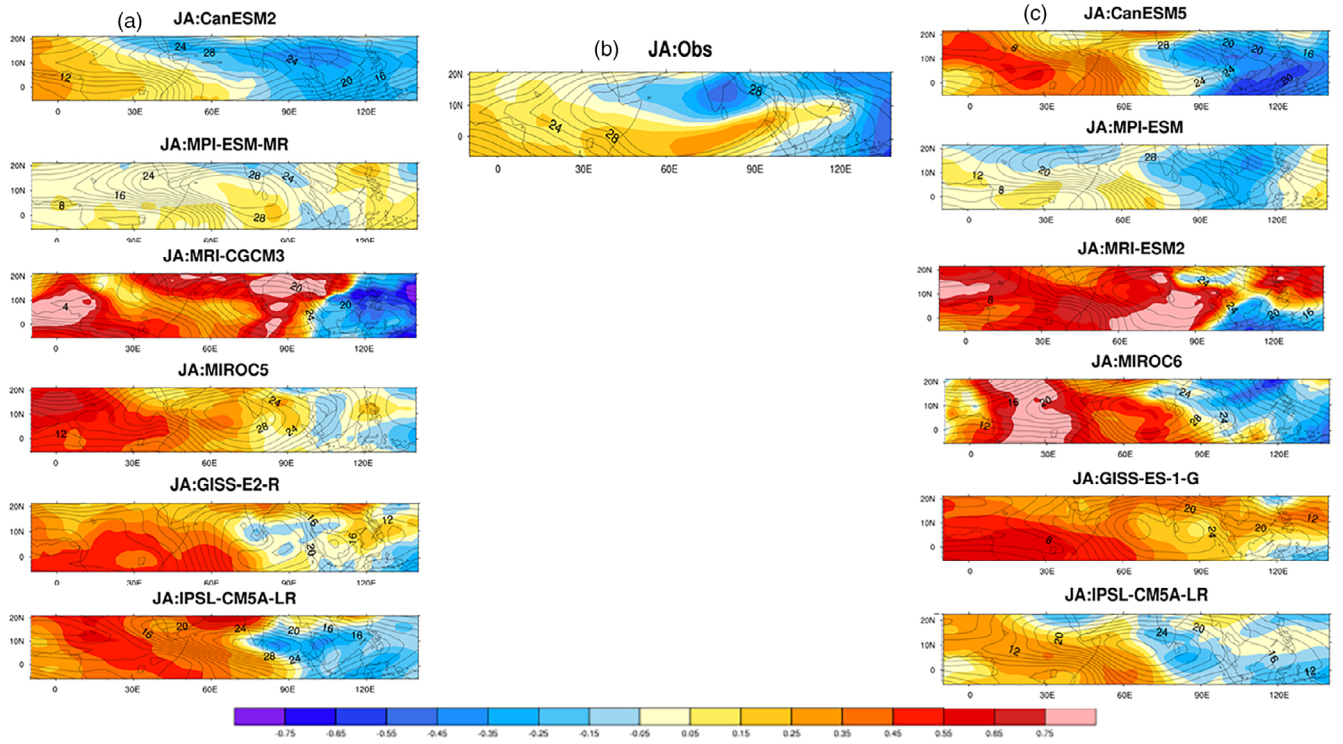

FIGURE 13 Correlation (based on absolute wind speed) between uBN precipitation and TEJ in JA for (a) CMIP5 models, (b) observation, and (c) CMIP6 models. Contour line is wind speed. Correlation coefficients with absolute value >0.264 are statistically significant at $p < .05$

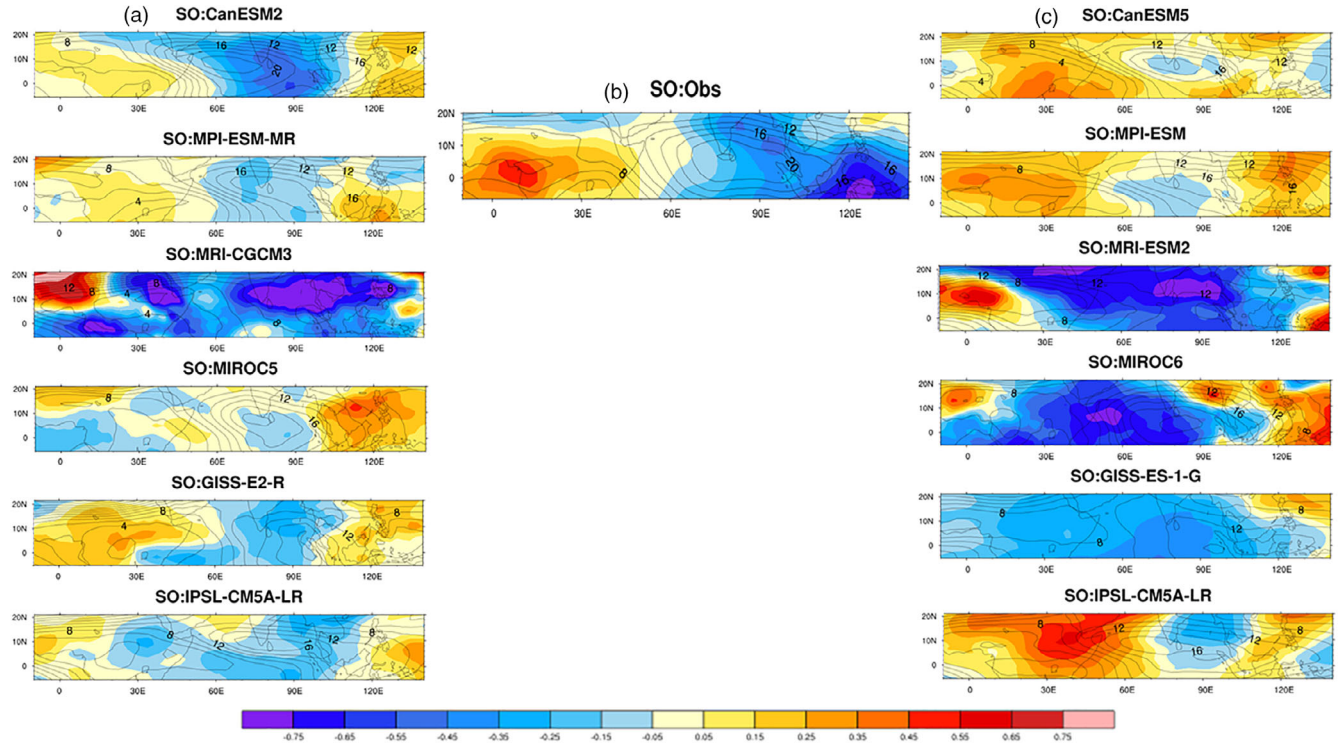

FIGURE 14 Correlation (based on absolute wind speed) between uBN precipitation and 150 hPa wind speed in SO (end of rainy season) of (a) CMIP5 models, (b) observation, and (c) CMIP6 models. Contour line is wind speed. Correlation coefficients with absolute value >0.264 are statistically significant at $p < .05$

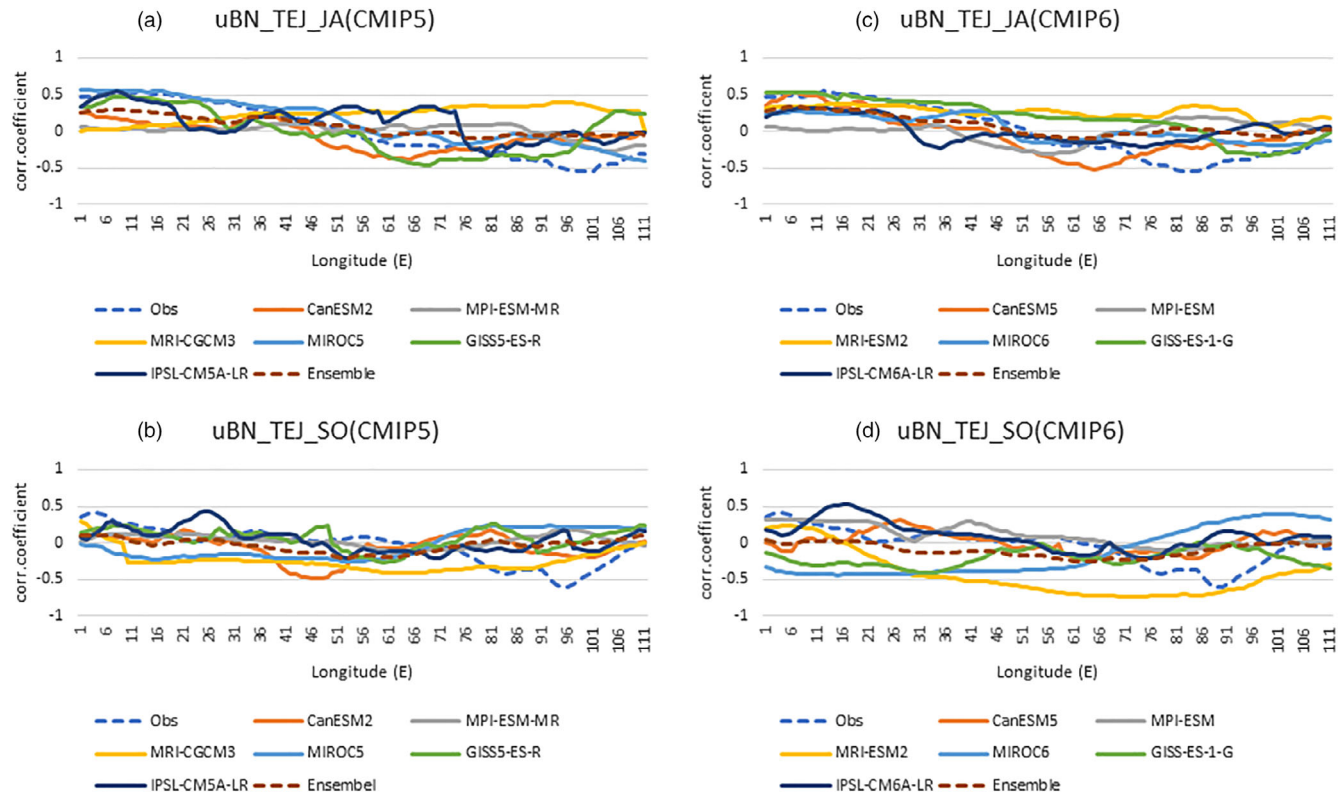

FIGURE 15 Longitudinal line plot showing uBN precipitation and TEJ correlation for (a, c) JA, averaged over 5°–15°N, and (b, d) SO, averaged over 2°–12°N, for (a, b) CMIP5 models and (c, d) CMIP6 models. Correlation coefficients with absolute value >0.264 are statistically significant at $p < .05$ for observations and for individual models

region, from the Horn of Africa across central and western Africa. This is sign-consistent with the divergence-convection hypothesis. Compared to JA, however, these positive correlations are lower and are more confined to the exit region, and they are generally statistically insignificant; weak negative correlations are observed in the TEJ core and the jet entry region, indicating that TEJ core strength alone is not a strong predictor of end-season precipitation in the uBN. Model representation of these associations is mixed. There is some evidence that in CMIP5 the CanESM2, MPI-ESM-MR, and GISS-E2-R models capture some elements of this pattern, while in CMIP6 there are features in CanESM5, MPI-ESM1-2-LR, and IPSL-CM6A-LR output, but there is no evidence that the CMIP6 ensemble captures these correlations better than the CMIP5 ensemble. We note that this analysis is subject to the poor coherence of signals in SO in general, with results representing a mix of contrasting September and October signals.

The representation of TEJ–uBN precipitation association across all models and for both JA and SO is summarized in Figure 15. The diversity of TEJ–uBN precipitation association between models is evident in both the CMIP5 and CMIP6 ensembles. Notably, the correlations between TEJ and uBN precipitation are positive from 45°E to 0°E and 70°E to 0°E in observation during JA (Figure 15a,c) and SO (Figure 15b,d), respectively. Similarly, most models also capture the patterns shown in the observation, but the magnitude of correlation is different.

5 | CONCLUSIONS

As a number of studies have confirmed, ENSO has a significant association with Ethiopian highlands precipitation variability. Most previous studies have focused on the summer season. The end of the rainy season, however, is important for agricultural activities of the uBN region, and drivers of variability in this season warrant full consideration. In this study we have examined GCM representations of precipitation for the peak (JA) and end (SO) of the uBN rainy season and quantified associations with ENSO and TEJ variability in historical simulations from the latest two generations of CMIP experiments: CMIP5 and CMIP6.

The majority of models from both CMIP5 and CMIP6 capture the negative association between ENSO and uBN rainfall in the peak of the rainy season. Correlations are weaker in most models than they are in observation, but there is a modest strengthening in the ensemble average of models from CMIP5 to CMIP6. The majority of simulations considered here (though not all) also capture the general spatial character of correlations in JA, with strong negative correlations in the western Ethiopian highlands, including the uBN, grading to positive correlations to the southeast.

Mechanistically, there are interesting differences between models and between CMIP5 and CMIP6 versions of models in the details of correlation patterns between ENSO, the TEJ, and uBN rainfall, but overall the results are relatively consistent with observation, and there is some evidence of ensemble-average improvement in representation of these proposed mechanisms in CMIP6 relative to CMIP5. Models do differ in their representation of ENSO–TEJ correlations, but as noted in Vashisht *et al*. (2021), models diverge much more considerably in representing uBN rainfall associations with the TEJ. This is unsurprising, to some extent, since the uBN is a small region, precipitation is a difficult variable for GCMs, and East Africa is generally an understudied region in which GCMs tend to have uneven performance.

Also, the connection between ENSO and uBN precipitation likely has multiple mediators, including possible influence of the Indian Monsoon via the Somali Jet or other atmospheric connections other than the TEJ (Camberlin, 1997; Diro *et al*., 2011; Gleixner *et al*., 2017). Indeed, while we find some upper-level wind patterns that are consistent with the hypothesized TEJ mediation of ENSO influence on uBN summertime rainfall, differences in model representation of the ENSO–TEJ association do not necessarily explain differences in model representation of ENSO–uBN correlations (Tables 3 and 4). For example, the GISS models show reasonably strong ENSO–uBN correlation in both CMIP5 and CMIP6, despite the fact that there is a major shift in representation of ENSO–TEJ correlations between generations of that model (Figure 12). CanESM, meanwhile goes from showing virtually no ENSO–uBN correlation in CMIP5 to having a strong correlation in CMIP6, when there is no dramatic change in TEJ-related correlations between those two models (Figures 12 and 14).

The end of the rainy season (SO) is a more complicated case, perhaps reflecting the transitional nature of this season. Most of the models included in our analysis do capture the weak negative association between ENSO an uBN rainfall in this season, including the fact that the weak negative relationship is the product of relatively strong negative correlations in September transitioning to a less clear relationship in October. October does prove to be a challenging month, however, as all of the CMIP5 models we considered and a majority of CMIP6 models show positive ENSO correlations with uBN rainfall in this month, while observations show a weak negative association. The spatial character of these relationships is also poorly captured by models in both CMIP5 and CMIP6 ensembles, and representation of the influence of TEJ—which is less than it is in JA, according to observations—is not consistent across models and does not show systematic improvement between CMIP5 and CMIP6. For ENSO correlation with TEJ, in fact, the

CMIP6 ensemble average appears to be further from observations than CMIP5.

The analyses presented in this study provide a snapshot of how a set of relatively high performing GCMs capture uBN rainfall, ENSO influence on uBN rainfall, and one of the leading proposed mechanisms for ENSO influence on the uBN, in the latest two coupled model intercomparison projects: CMIP5 and CMIP6. Our results indicate that the models perform reasonably well in JA. There is evidence of incremental improvement from CMIP5 to CMIP6, but overall the ensembles are comparable with respect to these metrics. We note that in limiting our study to models that perform relatively well for these metrics in CMIP5, we have set a high bar for demonstrating improvement. For the agriculturally important end-of-rains period (SO), GCM performance is mixed with respect to the metrics evaluated in this study. While the CMIP5 and CMIP6 ensembles offer similarly mixed performance with respect to precipitation totals and ENSO correlations with uBN precipitation, the fact that CMIP6 appears to underperform CMIP5 in the representation of ENSO–TEJ correlations warrants a deeper investigation. Overall, however, this study finds few systematic and meaningful differences between CMIP5 and CMIP6 in the representation of uBN precipitation variability and its relationship to ENSO. This implies that CMIP6 GCMs do not necessarily offer a more reliable future climate projections than those produced by the same set of high performing model families in the CMIP5 ensemble.

AUTHOR CONTRIBUTIONS

Zewdu Alamineh Fetene: Conceived and design the experiments; conceptualization; methodology; investigation; formal analysis; writing – review and editing original draft. Benjamin F. Zaitchik: Writing – review and editing original draft; fund acquisition; resources, conceptualization; methodology; investigation; supervision; project administration. Tadesse Terefe Zeleke and Baylie Damtie Yeshita: Supervision; review, writing and editing. Amandeep Vashisht: Resource; review, writing and editing.

ACKNOWLEDGEMENTS

The authors would like to express their sincere gratitude and appreciation to the Department of Earth and Planetary Sciences, John Hopkins University for hosting the first author as a visiting student and Physics Department, Bahir Dar University and Debre Tabor University for their collaborations with the first author during his travel. This research was supported by U.S. National Science Foundation (NSF) award ICER-1624335. We would like to thank the anonymous reviewers for their careful reading of our manuscript and their many insightful comments and suggestions.

CONFLICT OF INTEREST

The authors declare no potential conflict of interest.

ORCID

Zewdu Alamineh Fetene https://orcid.org/0000-0001-9806-8895

Amandeep Vashisht https://orcid.org/0000-0002-8414-2182

REFERENCES

Abtew, W., Melesse, A.M. and Dessalegne, T. (2009) El Niño Southern Oscillation link to the Blue Nile River basin hydrology. *Hydrological Processes*, 23(26), 3653–3660.

Ademe, D., Ziatchik, B.F., Tesfaye, K., Simane, B., Alemayehu, G. and Adgo, E. (2021) Observed and projected trends in climate extremes in a tropical highland region: an agroecosystem perspective. *International Journals of Climatology*, 42, 2493–2513. https://doi.org/10.1002/joc.7378.

Baker, N.C. and Huang, H.P. (2014) A comparative study of precipitation and evaporation between CMIP3 and CMIP5 climate model ensembles in semiarid regions. *Journal of Climate*, 27, 3731–3749.

Berhane, F., Zaitchik, B. and Dezfuli, A. (2014) Subseasonal analysis of precipitation variability in the Blue Nile River basin. *Journal of Climate*, 27(1), 325–344.

Bhattacharjee, P.S. and Zaitchik, B.F. (2015) Perspectives on CMIP5 model performance in the Nile River headwaters regions. *International Journal of Climatology*, 35, 4262–4275. https://doi.org/10.1002/joc.4284.

Block, C.P. and Strzepek, K. (2012) Economic analysis of large-scale Upstream River basin development on the Blue Nile in Ethiopia considering transient conditions, climate variability, and climate. *Journal of Water Resources Planning and Management*, 136(2), 156–166. https://doi.org/10.1061/ASCEWR.1943-5452.0000022.

Bokke, A.S., Taye, M.T., Willems, P. and Siyoum, S.A. (2017) Validation of general climate models (GCMs) over Upper Blue Nile river basin, Ethiopia. *Atmospheric and Climate Sciences*, 7, 65–75. https://doi.org/10.4236/acs.2017.71006.

Cai, W., Borlace, S., Lengaigne, M., Van Rensch, P., Collins, M., Vecchi, G., Timmermann, A., Santoso, A., McPhaden, J.M., Wu, L., England, M., Guilyardi, E., and Jin, F.F. (2014) Increasing frequency of extreme El Niño events due to greenhouse warming. *Nature Climate Change*, 4, 111–116. https://doi.org/10.1038/nclimate2100.

Camberlin, P. (1997) Rainfall anomalies in the source region of the Nile and their connection with the Indian summer monsoon. *Journal of Climate*, 10(6), 1380–1392.

Chen, H., Xu, C.Y. and Guo, S. (2012) Comparison and evaluation of multiple GCMs, statistical downscaling and hydrological models in the study of climate change impacts on runoff. *Journal of Hydrology*, 434, 36–45.

Chen, J., Brissette, F.P., Poulin, A. and Leconte, R. (2011) Overall uncertainty study of the hydrological impacts of climate change for a Canadian watershed. *Water Resources Research*, 47, W12509. https://doi.org/10.1029/2011WR010602.

Chen, T.C. and van Loon, H. (1987) Interannual variation of the tropica easterly jet. *Monthly Weather Review*, 115, 1739–1759.

Conway, D. and Hulme, M. (1993) Recent fluctuations in precipitation and runoff over the Nile sub-basins and their impact on main Nile discharge. *Climatic Change*, 25, 127–151.

Dibike, Y.B. and Coulibaly, P. (2006) Temporal neural networks for downscaling climate variability and extremes. *Neural Networks*, 19, 135–144.

Diro, G.T., Grimes, D.I.F. and Black, E. (2011) Teleconnections between Ethio-pian summer rainfall and sea surface temperature: part I. Observation and modelling. *Climate Dynamics*, 37, 103–119.

Emile-Geay, J., Cobb, K.M., Mann, M.E. and Wittenberg, A.T. (2013) Estimating central equatorial Pacific SST variability over the past millennium. Part II: reconstructions and implications. *Journal of Climate*, 26, 2329–2352.

Eyring, V., Bony, S., Meehl, G.A., Senior, C.A., Stevens, B., Stouffer, R.J. and Taylor, K.E. (2016) Overview of the Coupled Model Intercomparison Project Phase 6 (CMIP6) experimental design and organization. *Geoscientific Model Development*, 9, 1937–1958. https://doi.org/10.5194/gmd-9-1937.

Flohn, H. (1964) Investigations on the tropical easterly jet. *Bonner Meteorologische Abhandlungen*, 4, 1–83.

Funk, C., Nicholson, S.E., Landsfeld, M., Klotter, D., Peterson, P. and Harrison, L. (2015b) The centennial trends Greater Horn of Africa precipitation dataset. *Scientific Data*, 2, 150050.

Funk, C., Peterson, P., Landsfeld, M., Pedreros, D., Verdin, J., Shukla, S., Husak, G., Rowland, J., Harrison, L., Hoell, A., and Michaelsen, J. (2015a) The climate hazards infrared precipitation with stations—a new environmental record for monitoring extremes. *Scientific Data*, 2(1), 1–21.

Gleixner, S., Keenlyside, N., Viste, E. and Korecha, D. (2017) The El Niño effect on Ethiopian summer rainfall. *Climate Dynamics*, 49, 1865–1883. https://doi.org/10.1007/s00382-016-3421-z.

Grist, J.P. and Nicholson, S.E. (2001) A study of the dynamic factors influencing the rainfall variability in the West African Sahel. *Journal of Climate*, 14, 1337–1359. https://doi.org/10.1175/1520-0442(2001)014,1337:ASOTDF.2.0.CO;2.

Hastenrath, S. (1991) *Climate Dynamics of the Tropics*. Dordrecht, Boston: Kluwer Academic Publisher, p. 488.

IPCC. (2013) In: Stocker, T.F., Qin, D., Plattner, G.K., Tignor, M., Allen, S.K., Boschung, J., Nauels, A., Xia, Y., Bex, V. and Midgley, P.M. (Eds.) *Climate Change 2013. The Physical Science Basis Contribution of Working Group I to the Fifth Assessment Report of the Intergovernmental Panel on Climate Change*. Cambridge: Cambridge University Press.

Joseph, P.V. and Sabin, T.P. (2008) An ocean–atmosphere interaction mechanism for the active break cycle of the Asian summer monsoon. *Climate Dynamics*, 30, 553–566. https://doi.org/10.1007/s00382-007-0305-2.

Jury, M.R. (2015) Statistical evaluation of CMIP5 climate change model simulations for the Ethiopian highlands. *International Journal of Climatology*, 35, 37–44. https://doi.org/10.1002/joc.3960.

Kitoh, A. and Endo, H. (2016) Changes in precipitation extremes projected by a 20-km mesh global atmospheric model. *Weather and Climate Extremes*, 11, 41–52.

Kundzewicz, Z.W., Mata, L.J., Arnell, N.W., Döll, P., Jimenez, B., Miller, K., Oki, T., Şen, Z. and Shiklomanov, I. (2008) The implications of projected climate change for freshwater resources and their management. *Hydrological Sciences Journal*, 53(1), 3–10.

Le, J.A., El-Askary, H.M., Allali, M., Sayed, E., Sweliem, H., Piechota, T.C. and Struppa, D.C. (2020) Characterizing El Niño–Southern Oscillation effects on the Blue Nile yield and the Nile river basin precipitation using empirical mode decomposition. *Earth Systems and Environment*, 4(4), 699–711.

Miao, C., Duan, Q., Sun, Q., Huang, Y., Kong, D., Yang, T., Ye, A., Di, Z. and Gong, W. (2014) Assessment of CMIP5 climate models and projected temperature changes over northern Eurasia. *Environmental Research Letters*, 9, 055007.

Nicholson, S.E. (1995) Sahel, West Africa. *Encyclopedia of Environmental Biology*, 3, 261–275.

Nicholson, S.E. (2014) The predictability of rainfall over the Greater Horn of Africa. Part I: prediction of seasonal rainfall. *Journal of Hydrometeorology*, 15, 1011–1027. https://doi.org/10.1175/JHM-D-13-062.1.

Nicholson, S.E. and Klotter, D. (2021) The tropical easterly jet over Africa, its representation in six reanalysis products, and its association with Sahel rainfall. *International Journal of Climatology*, 41, 328–347. https://doi.org/10.1002/joc.6623.

Otieno, V.O. and Anyah, R.O. (2013) CMIP5 simulated climate conditions of the Greater Horn of Africa (GHA). Part I: Contemporary climate. *Climate Dynamics*, 41, 2081–2097. https://doi.org/10.1007/s00382-012-1549-z.

Pattanaik, D.R. and Satyan, V. (2000) Fluctuations of tropical easterly jet during contrasting monsoons over India: a GCM study. *Meteorology and Atmospheric Physics*, 75, 51–60.

Rao, S. and Srinivasan, J. (2016) The impact of latent heating on the location and strength of the tropical easterly jet. *Meteorology and Atmospheric Physics*, 128, 247–261. https://doi.org/10.1007/s00703-015-0407-z.

Shaman, J. and Tziperman, E. (2011) An atmospheric teleconnection linking ENSO and southwestern European precipitation. *Journal of Climate*, 24, 124–139. https://doi.org/10.1175/2010JCLI3590.1.

Siam, M.S. and Eltahir, E.A. (2017) Climate change enhances interannual variability of the Nile River flow. *Nature Climate Change*, 7, 350–354. https://doi.org/10.1038/nclimate3273.

Sivakumar, B. (2011) Global climate change and its impacts on water resources planning and management: assessment and challenges. *Stochastic Environmental Research and Risk Assessment*, 25, 583–600. https://doi.org/10.1007/s00477-010-0423-y.

Smith, T.M., Reynolds, R.W., Peterson, T.C. and Lawrimore, J. (2008) Improvements to NOAA's historical merged land–ocean surface temperature analysis (1880–2006). *Journal of Climate*, 21, 2283–2296. https://doi.org/10.1175/2007JCLI2100.1.

Sutcliffe, J.V. and Parks, V.P. (1999) *The hydrology of the Nile*. Wallingford: International Association of Hydrological Sciences IAHS special publication 5.

Taylor, K.E., Stouffer, R.J. and Meehl, G.A. (2012) An overview of CMIP5 and the experiment design. *Bulletin of the American Meteorological Society*, 93, 485–498. https://doi.org/10.1175/BAMS-D-11-00094.1.

Vashisht, A., Zaitchik, F.B. and Gnanadesikan, A. (2021) ENSO teleconnection to eastern Africa summer rainfall in global climate models: role of the tropical easterly jet. *Journal of Climate*, 34, 293–312.

Wang, B., Webster, P.J. and Teng, H. (2005) Antecedents and self-induction of the active-break Indian summer monsoon. *Geophysical Research Letters*, 32, L04704.

Wilby, R.L. and Wigley, T.M. (1997) Downscaling general circulation model output: a review of methods and limitations. *Progress in Physical Geography*, 21(4), 530–548.

Yang, S., Li, Z., Yu, J.Y., Hu, X., Dong, W. and He, S. (2018) El Niño–Southern Oscillation and its impact in the changing climate. *National Science Review*, 5, 840–857. https://doi.org/10.1093/nsr/nwy046.

Zaitchik, B.F., Simane, B., Habib, S., Anderson, M.C., Ozdogan, M. and Foltz, J.D. (2012) Building climate resilience in the Blue Nile/Abay highlands: a role for earth system sciences. *International Journal of Environmental Research*, 2012(9), 435–461. https://doi.org/10.3390/ijerph9020435.

Zappa, G., Shaffrey, L.C., Hodges, K.I., Sansom, P.G. and Stephenson, D.B. (2013) A multimodel assessment of future projections of North Atlantic and European extratropical cyclones in the CMIP5 climate models. *Journal of Climate*, 26, 5846–5862.

Zaroug, M.A., Eltahir, E.A. and Giorgi, F. (2014) Droughts and floods over the upper catchment of the Blue Nile and their connections to the timing of El Niño and La Niña events. *Hydrology and Earth System Sciences*, 18(3), 1239–1249.

Zeleke, T.T., Giorgi, G., Diro, G.T. and Zaitchik, B.F. (2017) Trend and periodicity of drought over Ethiopia. *International Journal of Climatology*, 37, 4733–4748. https://doi.org/10.1002/joc.5122.

SUPPORTING INFORMATION

Additional supporting information may be found in the online version of the article at the publisher's website.

How to cite this article: Fetene, Z. A., Zaitchik, B. F., Zeleke, T. T., Yeshita, B. D., & Vashisht, A. (2022). Coupled Model Intercomparison Project phase 5 and 6 representation of peak and end of rainy season over Upper Blue Nile basin. *International Journal of Climatology*, 1–20. https://doi.org/10.1002/joc.7736